PAPER • OPEN ACCESS

Overview of recent experimental results on the EAST Tokamak

View the article online for updates and enhancements.

Overview of recent experimental results on the EAST Tokamak

X. Gong[*] **on behalf of EAST Team and Collaborators**

The EAST Team: Yuntao Song[1], Baonian Wan[1], Jiangang Li[1], Yuanxi Wan[1], Xinchao Wu[1], Fukun Liu[1], Junling Chen[1], Jiansheng Hu[1], Guosheng Xu[1], Kun Lu[1], Xianzu Gong[1], Bingjia Xiao[1], Yu Wu[1], Xiang Gao[1], Damao Yao[1], Nong Xiang[1], Liqun Hu[1], Chundong Hu[1], Jiefeng Wu[1], Biao Shen[1], Ge Gao[1], Yiyun Huang[1], Liuwei Xu[1], Qiyong Zhang[1], Cheonho Bae[1], Bin Cao[1], Lei Cao[1], Jiafeng Chang[1], Dalong Chen[1], Ran Chen[1], Xiaojiao Chen[1], Yebin Chen[1], Yue Chen[1], Yunxin Cheng[1], Yong Cheng[1], Bojiang Ding[1], Fang Ding[1], Rui Ding[1], Shijun Du[1], Yanmin Duan[1], Jia Fu[1], Daming Gao[1], Wei Gao[1], Yongqi Gu[1], Bin Guo[1], Fei Guo[1], Yong Guo[1], Xiaofeng Han[1], Shiying He[1], Ailan Hu[1], Chang Hu[1], Guanghai Hu[1], Huaichuan Hu[1], Qingsheng Hu[1], Yanlan Hu[1], Zhenhua Hu[1], Juan Huang[1], Liansheng Huang[1], Ming Huang[1], Ronglin Huang[1], Xiang Ji[1], Hua Jia[1], Caichao Jiang[1], Yinxian Jie[1], Songqing Ju[1], Defeng Kong[1], Erzhong Li[1], Guoqiang Li[1], Jiahong Li[1], Junjun Li[1], Miaohui Li[1], Pan Li[1], Kedong Li[1], Shi Li[1], Yadong Li[1], Lizhen Liang[1], Yanchuan Liao[1], Shiyao Lin[1], Xin Lin[1], Bili Ling[1], Haiqing Liu[1], Huajun Liu[1], Jianwen Liu[1], Liang Liu[1], Shaocheng Liu[1], Sheng Liu[1], Wenbin Liu[1], Xiaoju Liu[1], Xiaoyan Liu[1], Yong Liu[1], Zhihong Liu[1], Zhimin Liu[1], Jianhua Lu[1], Zhengping Luo[1], Dengkui Ma[1], Huafeng Mao[1], Wendong Ma[1], Songtao Mao[1], Yuzhou Mao[1], Tingfeng Ming[1], Chao Pan[1], Chengkang Pan[1], Shengmin Pan[1], Jing Qian[1], Jinping Qian[1], Chengming Qin[1], Zhiyong Qiu[1], Qilong Ren[1], Zhicai Sheng[1], Shihua Song[1], Pengjun Sun[1], Xiaoyang Sun[1], Youwen Sun[1], Tian Tang[1], Ling Tao[1], Ang Ti[1], Baoguo Wang[1], Feng Wang[1], Fudi Wang[1], Huihui Wang[1], Jian Wang[1], Liang Wang[1], Linsen Wang[1], Mao Wang[1], Ping Wang[1], Xiaojie Wang[1], Shouxin Wang[1], Yating Wang[1], Yuehang Wang[1], Yong Wang[1], Zhengchu Wang[1], Jianglong Wei[1], Jing Wei[1], Xuechao Wei[1], Bin Wu[1], Dajun Wu[1], Hao Wu[1], Jinhua Wu[1], Xiangming Wu[1], Yibing Wu[1], Zege Wu[1], Weibin Xi[1], Tianyang Xia[1], Yezheng Xiao[1], Yahong Xie[1], Yuanlai Xie[1], Handong Xu[1], Liqing Xu[1], Liuwei Xu[1], Weiye Xu[1], Ning Yan[1], Rong Yan[1], Jianhua Yang[1], Lei Yang[1], Qingxi Yang[1], Yao Yang[1], Zhongshi Yang[1], Min Yu[1], Yaowei Yu[1], Qiping Yuan[1], Shuai Yuan[1], Qing Zang[1], Bin Zhang[1], Jian Zhang[1], Jizong Zhang[1], Liyuan Zhang[1], Ling Zhang[1], Ruirui Zhang[1], Shoubiao Zhang[1], Tao Zhang[1], Wei Zhang[1], Xinjun Zhang[1], Xiuqing Zhang[1], Yang Zhang[1], Zuchao Zhang[1], Hailin Zhao[1], Lianmin Zhao[1], Guoqiang Zhong[1], Ruijie Zhou[1], Haishan Zhou[1], Tianhu Zhou[1], Yue Zhou[1], Dahuan Zhu[1], Haisheng Zhu[1], Ping Zhu[1], Zeying Zhu[1], Huidong Zhuang[1], Zibo Zhou[1], Zhiyong Zhou[1], Zhiwei Zhou[1], Guizhong Zuo[1]

[*] Author to whom any correspondence should be addressed.

International and Domestic Collaborators: Huishan Cai[2], Weixing Ding[2], Tao Lan[2], Adi Liu[2], Wandong Liu[2], Shaojie Wang[2], Minyou Ye[2], Yi Yu[2], Ge Zhuang[2], Wei Chen[3], Guangjiu Lei[3], Lin Nie[3], Min Xu[3], Huang Yuan[3], Nanhua Yao[3], Zhe Gao[4], Long Zeng[4], Tieshuan Fan[5], Liu Chen[6,21], Guoyong Fu[6], Zhiwei Ma[6], Zengmao Sheng[6], Yong Xiao[6], Xiaogang Wang[7], Zhongyong Chen[8], Yonghua Ding[8], Xiwei Hu[8], Zijiang Wang[8], Fangchuan Zhong[9], Hongbin Ding[10], Dezhen Wang[10], Zhengxiong Wang[10], Chenggang Jin[11], Xuemei Wu[11], Xiaofei Yang[11], Jianhua Zhang[12], Qingyuan Hu[12], Xi Yuan[12], Changqi Chen[13], Shuyi Gan[13], Xudi Wang[13], Congzhong Wu[13], Chongwei Zhang[13], Ting Zhang[13], Wu Zhu[13], Erhua Kong[14], Kaisong Wang[14], Chuanli Wang[14], Hongtao Yang[14], Lixiang Zhang[14], Yuhong Xu[15], Paul Anderson[16], Gheni Abla[16], Vincent Chan[16], John L. Doane[16], Andrea Garofalo[16], Punit Gohil[16], Chung Lih Hsieh[16], Ruey Hong[16], David Humphreys[16], Alan Walter Hyatt[16], Gary Jackson[16,5], Lang Lao[16], Yueqiang Liu[16], James Leuer[16], John Lohr[16], Mohamad Ali Mahdavi[16], Robert Olstad[16], Ben Penaflor[16], Ron Prater[16], David Piglowski[16], Michael Schaffe[16], Tim Scoville[16], Wayne Solomon[16], Mike Walker[16], Anders Welander[16], Manfred Bitter[17], Robert Budny[17], Robert A. Ellis[17], Nat Fisch[17], Rich Hawryluk[17], Kenneth W. Hill[17], Joel Hosea[17], Michael A. Jaworski[17], Egemen Kolemen[17], Rajesh Maingi[17], Dennis Mansfield[17], Dana M. Mastrovito[17], Jonathan Menard[17], Dennis Mueller[17], Novmir Pablant[17], Lane Roquemore[17], Filippo Scotti[17], Gary Taylor[17], Kevin Tritz[17], Randy Wilson[17], Michael Zarnstorff[17], Seung Gyou Baek[18], Beck Bill[18], Paul T. Bonoli[18], Robert Granetz[18], Ron Parker[18], Shunichi Shiraiwa[18], Josh Stillerman[18], Greg Wallace[18], Stephen Wukitch[18], Lihua Zhou[18], He Huang[19], Kenneth Gentle[19], Ken Liao[19], Perry Philippe[19], William L. Rowan[19], Linjin Zheng[19], Patrick H. Diamond[20], George R. Tynan[20], Nicolas Fedorczak[20], Peter Manz[20], Lei Zhao[20], David Brower[21], William W. Heidbrink[22], Yubao Zhu[22], Calvin W. Domier[23], Neville C. Luhmann[23], Chris Holcomb[24], Xueqiao Xu[24], Eric Wang[24], Max E. Fenstermarcher[24], Mickey Wade[24], Donald L. Hillis[25], Steve Meitner[25], Mickey Wade[25], Igor V. Vinyar[26], Vladimir Davydenko[27], Igor Shikhovtsev[27], Naoko Ashikawa[28], Kasahara Hiroshi[28], Katsumi Ida[28], Shinichiro Kado[28], Tomita Kawamura[28], Saito Kenji[28], Ryuhei Kumazawa[28], Ogawa Kunihiro[28], Isobe Mitsutaka[28], Shigeru Morita[28], Haruhisa Nakano[28], Masaki Osakabe[28], Mizuki Sakamoto[28], Yasuhiko Takeiri[28], Kazuo Toi[28], Katsuyoshi Tsumori[28], Nobuta Yuji[28], Masaya Hanada[29], Mitsuru Kikuchi[29], Atsushi Kojima[29], Kazuhiro Watanabe[29], Jean-Francois Artaud[30], Vincent Basiuk[30], F. Bouquey[30], B. Bremond[30], Laurent Colas[30], Joan Decker[30], D. Douai[30], Annika Ekedahl[30], Christel Fenzi[30], Eric Gauthier[30], Gerardo Giruzzi[30], Marc Goniche[30], Dominique Guilhem[30], Walid Helou[30], Julien Hillairet[30], Tuong Hoang[30], Philippe Huynh[30], Frederic Imbeaux[30], Xavier Litaudon[30], Roland Magne[30], Yves Peysson[30], K. Vueillie[30], Xiaolan Zou[30], Alberto Loarte[31], Richard Pitts[31], Tom Wauters[31], Franz Braun[32], R. Bilato[32], Volodymyr Bobkov[32], J.M. Noterdaeme[32], Qingquan Yu[32], Yunfeng Liang[33], Jonny Pearson[33], Michael Rack[33], Joseph Banks[34], John Fessey[34], Charles Monroe[34], Damian King[34], Stefan Schmuck[34], Hongjuan Sun[34], Paul Trimble[34], Tom Todd[34], Jun-Gyo Bak[35], Suk-Ho Hong[35], Sangong Lee[35], Bae Young Soon[35], Oh Byung Hoon[36], Chang Doo Hee[36], Lee Kwang Won[36], Luca Amicucci[37], Giuseppe Calabro[37], Silvio Ceccuzzi[37], Roberto Cesario[37], Flavio Crisanti[37], Edmondo Giovannozzi[37], Giuseppe Ramogida[37], Gianmaria De Tommasi[37], Angelo Antonio Tuccillo[37], Bruno Viola[37], Raffaele Albanese[38], Roberto Ambrosino[38], Lucio Barbato[38], Stefano Mastrostefano[38], Alfredo Pironti[38], Vincenzo Pericoli Ridolfini[38], Rory Scannell[38], Fabio Villone[38], Volker Naulin[39], Anders H. Nielsen[39], Roman Zagorsky[40], Sandor Zoletnik[41], Chijin Xiao[42], B.Madsen[43], M. Salewski[43] Eugenio Schuster[44]

[1] Institute of Plasma Physics, Chinese Academy of Sciences, Hefei 230031, China

[2] University of Science and Technology of China, Hefei 230026, China

[3] Southwestern Institute of Physics, Chengdu 610041, China

[4] Tsinghua University, Beijing, China

[5] Peking University, Beijing, China

[6] Zejiang University, Hangzhou, China

[7] Harbin Institute of Technology, Harbin 150001, China

[8] Huazhong University of Science and Technology, Wuhan, China

[9] Donghua University, Shanghai, China

[10] Dalian University of Technology, Dalian 116024, China

[11] Soochow University, Shuzhou, China

[12] China Academy of Engineering Physics, Mianyang 621900, China

[13] Hefei University of Technology, Hefei 230009, China

[14] Anhui University of Science and Technology, Huainan 232001, China

[15] Southwest Jiaotong University, Chengdu 611756, China

[16] General Atomic, San Diego, CA 92186-5608, United States of America

[17] Princeton Plasma Physics Laboratory, PO Box 451, Princeton, NJ 08543, United States of America

[18] Massachusetts Institute of Technology, Plasma Science and Fusion Center, Cambridge, MA 02139, United States of America

[19] Fusion Research Center, University of Texas at Austin, Austin, TX 78712, United States of America

[20] University of California, San Diego, CA 92093, United States of America

[21] University of California Los Angeles, Los Angeles, CA 90095, United States of America

[22] University of California at Irvine, Irvine, CA 92697, United States of America

[23] University of California at Davis, Davis, CA 95616, United States of America

[24] Lawrence Livermore National Laboratory (LLNL), Livermore, CA 94551, United States of America

[25] Oak Ridge National Laboratory, Oak Ridge, TN 37831-6169, United States of America

[26] PELIN, LLC, 27A, Gzhatskaya, Saint Petersburg 195220, Russian Federation

[27] Budker Institute of Nuclear Physics, Novosibirsk 630090, Russian Federation

[28] National Institute for Fusion Sciences, Toki 509-5292, Japan

[29] National Institute for Quantum and Radiological Science and Technology, Fusion Energy Research Development Directorate, Naka, Japan

[30] CEA Cadarache, IRFM, F-13108 Saint Paul-lez-Durance, France

[31] ITER Organization, Route de Vinon sur Verdon, 13115 St Paul Lez Durance, France

[32] Max-Planck Institute for Plasma Physics, D-85748, Garching, Germany

[33] Association EURATOM-FZJ, D-52425 Jülich, Germany

[34] Euratom/CCFE Fusion Association, Culham Science Centre, Abingdon, Oxon OX14 3DB, United Kingdom of Great Britain and Northern Ireland

[35] National Fusion Research Institute, Yuseong-Gu, Daejeon, 305-806, Korea, Republic Of

[36] Korea Atomic Energy Research Institute, Yuseong-Gu, Daejeon, 305-353, Korea, Republic Of

[37] ENEA Unità Tecnica Fusione, C.R. Frascati, Via E. Fermi 45, 00044 Frascati, Roma, Italy

[38] CREATE, Università di Napoli Federico II, Università di Cassino and Università di Napoli Parthenope, Via Claudio 19, 80125 Napoli, Italy

[39] Association Euratom-Risø DTU, Roskilde, Denmark

[40] Institute of Plasma Physics and Laser Microfusion, Warsaw, Poland

[41] Association EURATOM—KFKI RMKI, P.O. Box 49, H-1525 Budapest, Hungary

[42] University of Saskatchewan, Saskatoon, Saskatchewan S7N 5E5, Canada

[43] Department of Physics, Technical University of Denmark, Kgs. Lyngby, Denmark

[44] Plasma Control Laboratory, Lehigh University, Bethlehem, PA 18015-3085, United States of America

E-mail: xz_gong@ipp.ac.cn

CrossMark

Abstract

Since the last IAEA-FEC in 2021, significant progress on the development of long pulse steady state scenario and its related key physics and technologies have been achieved, including the reproducible 403 s long-pulse steady-state H-mode plasma with pure radio frequency (RF) power heating. A thousand-second time scale ($\sim$1056 s) fully non-inductive plasma with high

injected energy up to 1.73 GJ has also been achieved. The EAST operational regime of high β_P has been significantly extended ($H_{98y2} > 1.3$, $\beta_P \sim 4.0$, $\beta_N \sim 2.4$ and $n_e/n_{GW} \sim 1.0$) using RF and neutral beam injection (NBI). The full edge localized mode suppression using the $n = 4$ resonant magnetic perturbations has been achieved in ITER-like standard type-I ELMy H-mode plasmas with $q_{95} \approx 3.1$ on EAST, extrapolating favorably to the ITER baseline scenario. The sustained large ELM control and stable partial detachment have been achieved with Ne seeding. The underlying physics of plasma-beta effect for error field penetration, where toroidal effect dominates, is disclosed by comparing the results in cylindrical theory and MARS-Q simulation in EAST. Breakdown and plasma initiation at low toroidal electric fields (<0.3 V m^{-1}) with EC pre-ionization is developed. A beneficial role on the lower hybrid wave injection to control the tungsten concentration in the NBI discharge is observed for the first time in EAST suggesting a potential way toward steady-state H-mode NBI operation.

Keywords: steady state long pulse, EAST tokamak, ITPA

(Some figures may appear in colour only in the online journal)

1. Introduction

The EAST (major radius $R \leqslant 1.9$ m, minor radius $a \leqslant 0.45$ m, plasma current $I_p \leqslant 1$ MA, toroidal field $B_T \leqslant 3.5$ T) research program has been instrumental in developing the scientific basis to project integrated solutions of steady-state long pulse in supporting future fusion devices [1–4]. To meet this goal, more heating and current drive (CD) powers are equipped such as an additional Electron Cryotron Resonant Heating (ECRH) gyrotron, a new two-strap Ion Cryotron Resonant Frequency (ICRF) antenna with lower $k_\parallel$ spectrum and the change of counter-current neutral beam injection (NBI) system to the co-current direction for more efficient heating and CD with lowering a large fraction of the fast-ion losses. In addition, the EAST lower divertor has completed the upgrade from graphite divertor to tungsten divertor [2], leading to the increase of steady-state heat exhausting capacity of the lower divertor from 2 to 10 MW m^{-2}.

Since the 2021 IAEA FEC, EAST experiments have been carried out in support of high-performance steady-state operation and physics understanding for ITER and CFETR. The first demonstration of reproducible 403 s long-pulse steady-state H-mode plasma with $H_{98y2} > 1.3$, $\beta_P \sim 2.5$, $\beta_N \sim 1.6$, $n_e/n_{GW} \sim 0.7$ and a good control of impurity and heat exhaust have been achieved on EAST using the pure radio frequency (RF) power heating and CD. In support of ITER and CFETR long pulse operation, a thousand-second time scale ($\sim$1056 s) fully non-inductive plasma has been achieved. The recent achievements in the long-pulse high performance scenario development are discussed in section 2. Section 3 presents the key issues and relevant physics understanding in the long-pulse operation regime, including power and particle handling, shape control, high-Z impurity and heat flux control. Recent results contributed to ITPA is given in section 4, including inductive scenario, high beta operation, ELM control, Error field analysis, EC pre-ionization and assisted startup, ITER-like fast ramp down and Material erosion. A summary and future plan for the EAST program are described in section 5.

2. Progress of EAST in support of ITER and CFETR

On EAST, the steady state long pulse plasmas have been developed towards more ITER-relevant conditions, such as low torque injection, RF-dominated heating and CD at high density with an ITER-like tungsten divertor. A duration of 403 s H-mode plasmas ($I_p = 300$ kA, $H_{98y2} > 1.3$, $\beta_P \sim 2.5$, $\beta_N \sim 1.6$ and $n_e/n_{GW} \sim 0.7$) have been achieved and perfectly reproduced by exploiting the improved long pulse capabilities in EAST (shown in figure 1), with the q profile and plasma pressure distribution given in figure 2. The integration of good control of impurities, recycling, core/edge MHD stability, and heat flux exhaust is demonstrated. A high frequency ($\sim$100–200 Hz), small amplitude ELMs regime facilitates the RF power coupling to the H-mode edge. Low tungsten concentration ($C_w < 10^{-5}$) in these high-β_P plasmas benefits from the on-axis ECRH-heating. The loop voltage with the target to zero was feedback controlled by the actuator of 4.6 GHz lower hybrid wave (LHW).

In support of ITER and CFETR long pulse operation, a thousand-second time scale ($\sim$1056 s) fully non-inductive plasma (shown in figure 3) was achieved [5]. It is Super I-mode, which is characterized by the coexistence of an electron internal transport barrier (ITB) at the plasma center and an improvement energy confinement mode (I-mode) [6], without ELMs at the plasma edge. A total energy of 1.73 GJ was injected into the plasma. Plasma was operated at $I_p = 330$ kA and $\bar{n}_e = 1.8 \times 10^{19}$ m^{-3} with a total RF power of 1.65 MW (1.1 MW of LHCD at 4.6 GHz, and 0.55 MW of ECRH). As shown in figure 3, all the main plasma parameters are stationary during the discharge. The radiation power, with tungsten (W) as the major radiating species, is found to be very low ($\sim$150 kW). Note that the discharge is fully non-inductive. Key technical and scientific challenges including robust plasma shape control, improvement of magnetic measurements, plasma ramp-up/down, particle and heat load exhaust over 1000 s have been addressed. A powder dropper [7] was used to inject lithium to mitigate impurities and reduce recycling, which allows control of density and radiated
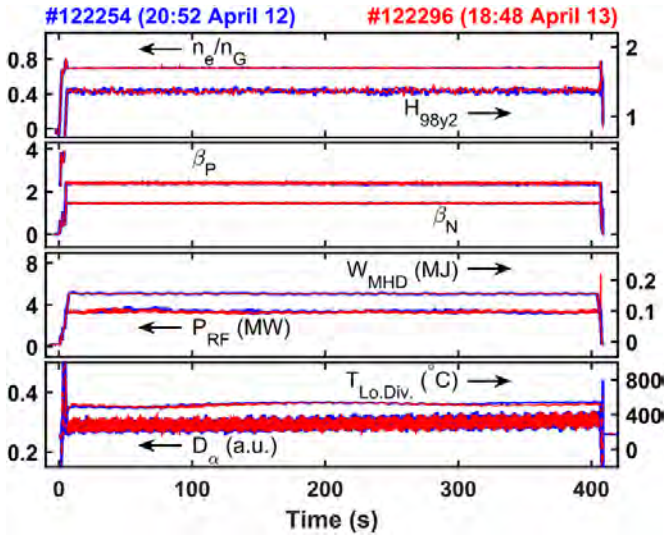
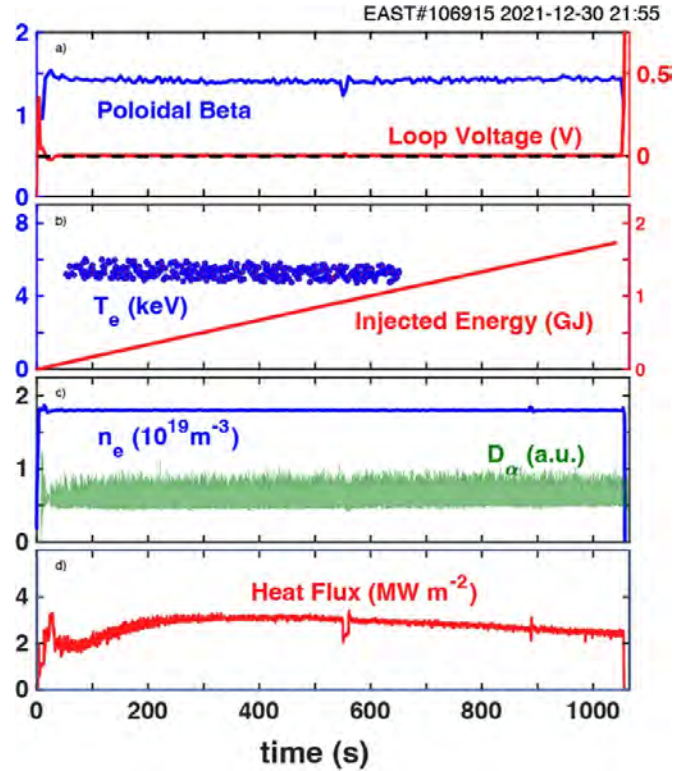**Figure 1.** Time traces of key parameters of long pulse H-mode plasmas, from top to bottom are the Greenwald fraction (n_e/n_G), confinement enhancement factor (H_{98y2}), poloidal beta (β_P), normalized beta (β_N), plasma stored energy (W_{MHD}), injected power of RF (P_{RF}), peak temperature on lower divertor ($T_{Lo.Div.}$) and D_α signal.
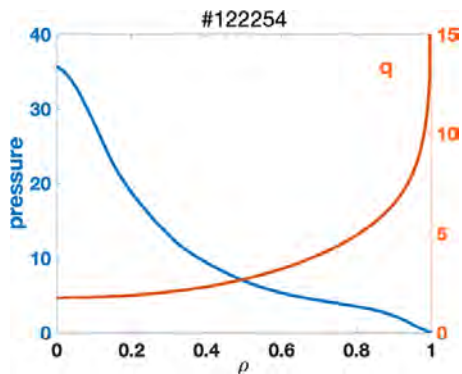
Figure 2. Profiles for plasma pressure and safety factor (q) for discharge 122254. The horizontal axis is the normalized toroidal flux.

Figure 3. Time traces of the thousand-second discharge #106915. (*a*) Poloidal beta and loop voltage, (*b*) core electron temperature and injected energy, (*c*) line averaged density and D_α signal, (*d*) peak heat flux on the divertor target.
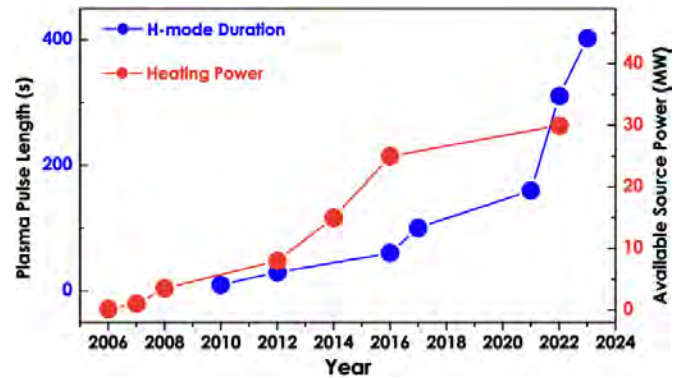
Figure 4. Progress of long pulse H-mode plasma on EAST.

power due to impurities. Note that low particle recycling is favorable for cryo-pumping, which does not suffer from saturation or release of particles back into the plasma when in a low recycling regime. In addition, the plasma control system (PCS) including the integrator drift were routinely tested before the daily experiments to minimize the error due to the offset of integrators of magnetic measurements, which is essential for controlling the plasma configuration.

Aiming at establishing the scientific basis for integrated solutions, including high confinement and bootstrap current fraction, high RF CD at high density and core-edge integration of steady-state operation, EAST team members have made continuous and substantial efforts in exploring long pulse high confinement steady-state plasma operation regimes (shown in figure 4) in the past two decades.

3. Key issues and relevant physics understanding in long-pulse operation regime

In EAST, several key technical challenges related to the development of long pulse operation have been investigated. The important topics including power and particle handling, shape control, high-Z impurity and heat flux control, are addressed.

3.1. Augmentation of heating and CD capability

It is recognized that LHCD efficiency increases significantly with the volume-averaged electron temperature $<T_e>$. According the CD theory, higher T_e corresponds to higher
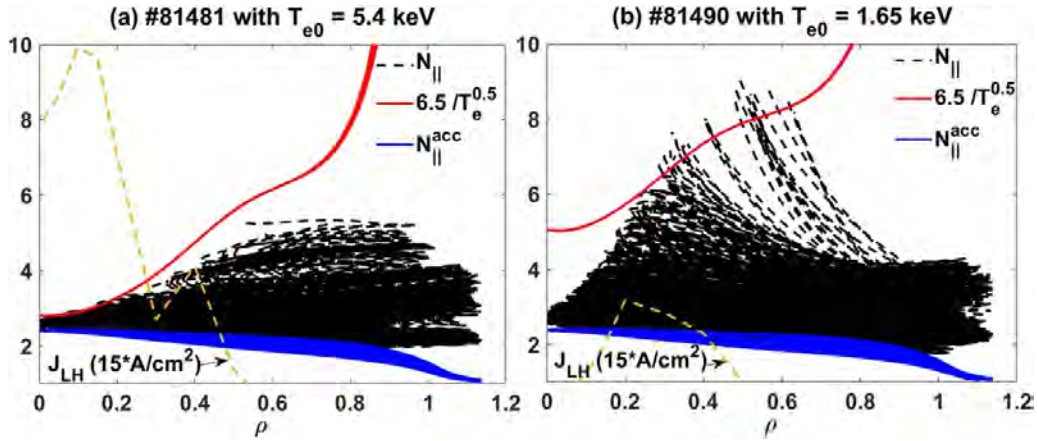
Figure 5. $N_\parallel$ pattern (black lines) along the ray trajectories calculated by GENRAY code versus the normalized radius ρ. The red lines correspond to the local condition of linear Landau damping $N_\parallel = 6.5/T_e^{0.5}$(keV). The blue lines correspond to the local accessibility criterion ($N_\parallel^{acc}$). The yellow dashed lines represent the LH current density profiles predicted by GENRAY code.
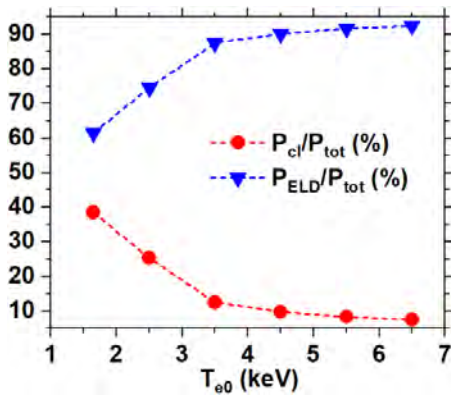
Figure 6. Power ratio of the collisional dissipation in the edge (P_{cl}) and the electron Landau damping in the core (P_{ELD}) to the total power (P_{tot}) as a function of T_{e0}.

velocity of resonant electrons, which means lower collisionality, thus leading to higher CD efficiency. Ray-tracing simulations show that higher electron temperature produced by ECRH can shorten the spectral gap between the parallel refractive index ($N_\parallel$) required for Landau damping (namely, $N_\parallel = 6.5/T_e^{0.5}$(keV), as indicated by the red lines) and the launched $N_\parallel$ (=2.26), as shown in figure 5 [8]. Hence, fewer passes (suggested by the number of black lines) are needed before the power is fully absorbed, leading to less power absorption in the SOL by collisional damping. As illustrated in figure 6, the power fraction of collisional dissipation to the total power decreases with increasing T_{e0}.

The ICRF wave coupling has an exponential relationship with the antenna to the fast wave cut-off layer. The lower wave spectrum is an effective way to improve the coupling without actively changing the plasma distribution. The coupling of the antenna has been significantly improved by optimizing the antenna wave spectrum on EAST, including the L- and H-mode discharge (shown in figure 7), which overcomes the problem of limiting the power of the antenna due to insufficient antenna coupling of the original antenna [9, 10]. At the

same time, it is observed that the heating effect of the new antenna has been significantly improved (figure 8).

3.2. Power and particle handling

In the EAST long pulse operation, the plasma density was feedback controlled via Supersonic Molecular Beam Injection (SMBI) fuelling. An example is shown in figure 9. The global fuel recycling was still controlled successfully to ∼0.95–0.97 as shown in figure 9(*b*), and the particle was mainly controlled by improved divertor pumping and lithium wall conditioning, which play the key role in sustaining the constant plasma density for over 1000 s. The new water-cooled lower divertor provides sufficient heat removal capability for long pulse discharges. The temperature of lower divertor was kept in the range of 300 °C–500 °C during the 1056 s plasma as shown in figure 9(*c*). Moreover, the new flat-type structure shows better heat exhaust than the monoblock one, the temperature of the flat-type divertor was obviously lower than that of monoblock divertor by ∼160 °C. The good control of divertor temperature is also useful for the particle control during the long pulse discharges. As shown in figure 3, the heat flux on the divertor target increased from 50 s to about 350 s and decreased after 350 s. It is mainly because the gas puff, pumping and global recycling were not constant but in a relatively dynamic balancing state, which influences the particle balance in the SOL region, as shown in figure 9.

3.3. Plasma position and shape control

High-performance long pulse discharges require accurate and robust shape control. The ISO-FLUX control scheme has been adopted for the EAST shape control [11]. The control segments and X-points are set as shown in figure 10(*b*). The control points are determined by the intersection of the control segments and target boundary, and the difference in the magnetic flux between each control point and the active X-point is compensated. A parallel real-time equilibrium reconstruction code called PEFIT [12] is used to calculate the

Figure 7. N-port and original antenna coupling resistance with different plasma line averaged densities, where the H-mode scenarios are the combination with ICRF + LHW + ECH.

Figure 8. Contribution of old and new antennas to plasma stored energy as a function of antenna power.

Figure 9. Plasma parameters of shot#106915, (*a*) Plasma density (blue) and D_α emission (green), (*b*) injection rate of SMBI (red) and global recycling coefficient (R_{global}), (*c*) surface temperature of flat-type divertor (red) and monoblock divertor (blue). For the lower divertor, 3/4 of targets in toroidal direction are monoblock structure and others are flat-type divertor.

3.4. High-Z impurity and heat flux control

3.4.1. Transport and control of tungsten impurity. In recent two years, behavior of high-Z impurity is studied combining with experiment and simulation. To understand the underlying physics, the tungsten transport in hybrid discharges is studied using the integrated modeling. The result indicates the tungsten accumulation is caused by a large neoclassical pinch, which may be originated in the density peaking and in the change of toroidal rotation [16]. The measured tungsten impurity profile indicates an effective suppression of the tungsten ions from core plasmas in NBI discharges with LHW [17], as shown in figure 11. The transport coefficient of tungsten impurity with and without LHW injection and at high toroidal rotation velocity has been simulated by TYGRO. It can be seen from figure 12 that during the LHW phase, the turbulent diffusion of tungsten is enhanced while the neoclassical convection is weakened. The simulated results also reve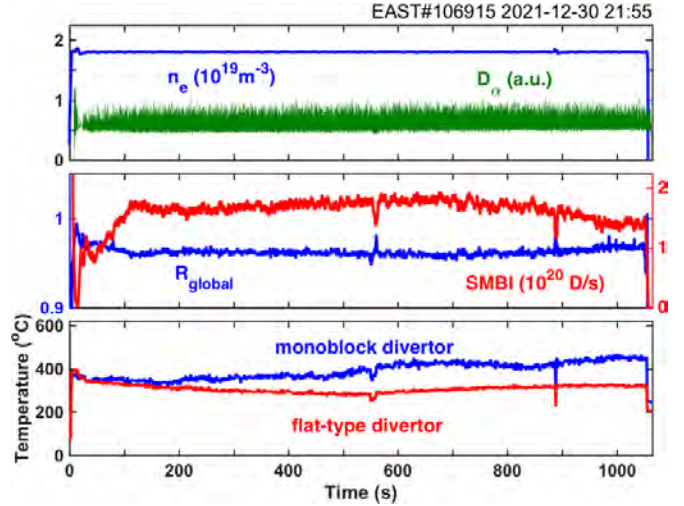al that the toroidal rotation increases the neoclassical convection and leads to the inward pinch of tungsten. Therefore, LHW affects tungsten impurity transport in two ways: LHW heating causes an increase in the turbulent diffusion of tungsten by increasing the electron temperature. Meanwhile, it decreases the plasma toroidal rotation velocity and reduces the inward neoclassical convection of tungsten. For the effect of on-axis RF (ECRH and LHW) heating on the tungsten transport, the modeling result suggests a key role on electron temperature and its gradients in generating a large turbulent diffusion which can increase the growth rate of instability [18].

3.4.2. Compatibility of divertor detachment with core confinement. The excessively high heat load on the divertor target plates is a critical challenge for tokamak operation with high performance. Radiative divertor detachment with

magnetic flux on each control point and X-point from the magnetic measurements. A series of advanced vertical position control algorithms [13, 14] are applied on EAST to ensure the robustness of shape and position control. To minimize the influence of zero drift on magnetic measurements, new fiber optic current sensors are used for plasma and coil current measurements, and a linear drift deduction algorithm is developed in the PCS [15]. During the long-pulse experiment, the steady-state control error of each control point is smaller than 2 mm, and for the X-point is smaller than 5 mm (as shown in figure 10(*a*)). To reduce the output power of the poloidal field (PF) power supplies, the PF coils' currents are optimized by changing the steady-state plasma flux as shown in figure 10(*c*), which can be controlled by adjusting the timing of LHW.
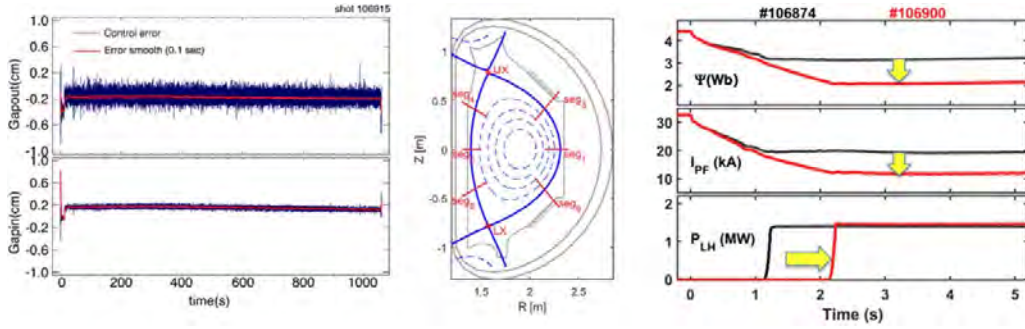
Figure 10. (*a*) Shape control error of inner and outer gap for shot 106915. Gapin/gapout is the distance between the separatrix and the first wall in the high-field-side/low-field-side mid-plane. (*b*) Control segments (red line) and X-points (red star) in double-null ISOFLUX control scheme. (*c*) Poloidal coil current evolution change with tuning LHW timing, for which the ψ is the poloidal flux with the unit of Wb, I_{PF} is the sum of the poloidal coils current, and P_{LH} is the power of LHW.
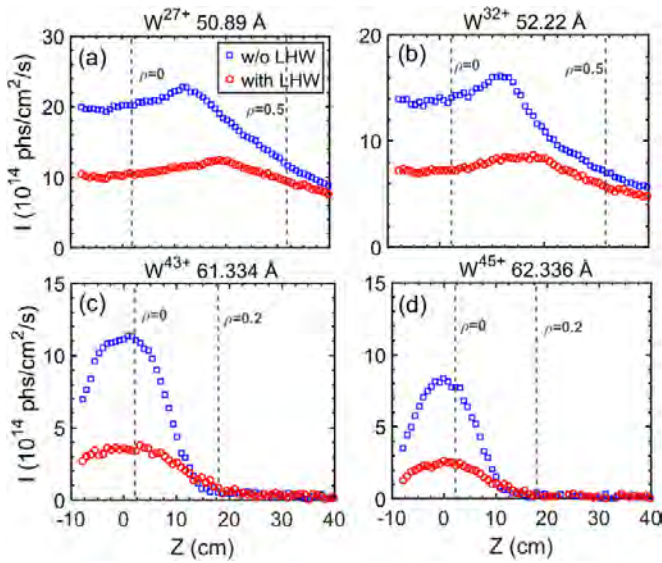
Figure 11. Vertical intensity profile of (*a*) W^{27+} (50.89 Å), (*b*) W^{32+} (52.22 Å), (*c*) W^{43+} (61.334 Å) and (*d*) W^{45+} (62.336 Å) in W-UTA spectra during H-mode phase without LHW and with LHW in shot #70769. The radial locations of $\rho = 0$, $\rho = 0.2$ and $\rho = 0.5$ are indicated with vertical dash lines.

impurity seeding is one of the most promising means for the control of heat flux. The divertor partial detachment with high-confinement core plasma has been achieved by using mixed neon (Ne) and deuterium (D$_2$) seeding in EAST with ITER-like tungsten divertor [19, 20]. Both the plasma stored energy and $H_{98,y2} > 1.1$ are maintained, with the divertor electron temperature, heat flux and the surface temperature near the strike point being all significantly reduced. To achieve the compatibility of divertor detachment and core confinement, the off-normal events should be monitored, including excessive impurity seeding, loss of heating and dust droplets. Therefore, a module of stored-energy monitoring to ensure stable plasmas in EAST long-pulse detachment feedback operation was developed [21]. The compatibility of divertor partial detachment and good energy confinement is demonstrated by active impurity seeding (50% Ne, 50% D$_2$). By employing the new lower W divertor, the active detachment feedback control compatible with core plasma confinement via the electron temperature on the divertor target T_{et} controller has been extended to 30 s long-pulse H-mode operation, with active detachment-control duration being 25 s [22].

In addition to the steady-state heat fluxes on the divertor target, the sustained large ELM control and stable partial detachment have been achieved concurrently with Ne seeding in EAST [23]. With Ne seeding, the electron temperature T_{et} around the lower outer strike point decreases from more than 70 eV during the large ELM burst to less than 5 eV in the stable ELM-free phase, as shown in figure 13. The transient heat flux around the lower outer strike point in the ELM-free state after Ne seeding decreases by more than 90% compared with that during large ELM burst before Ne seeding. A slight improvement of plasma confinement is observed in the partially detached state, mainly attributed to the increased electron density and ion temperature in the core region. The increase of T_i is mainly attributed to the stabilizing effect of impurity on the turbulences in the core region, including trapped electron mode (TEM) and the ion temperature gradient (ITG) [24]. In the pedestal region, the density gradient and the electron temperature show subtle variation. The effective charge number Z_{eff} increases from 1.3 in attached state to 2.3 in detached state after Ne seeding, leading to a decrease in the edge bootstrap current and the pedestal pressure gradient, and thus the stabilization of ELMs.

4. Recent results contributed to the ITPA

4.1. Inductive scenario

Parallel to the steady state long-pulse scenario development, the improved confinement at low $q_{95} < 3.5$ operation regime with fishbone instability compared to sawtooth oscillation has been observed and investigated on EAST under dominant electron heating condition with tungsten divertor (shown in figure 14) [25]. The formation of ITB in ion thermal channel is found to strongly correlate to the trigger of fishbone, accompanying by reduced particle outward transport in the center identified by core peaked density profile. Current density distribution is changed from
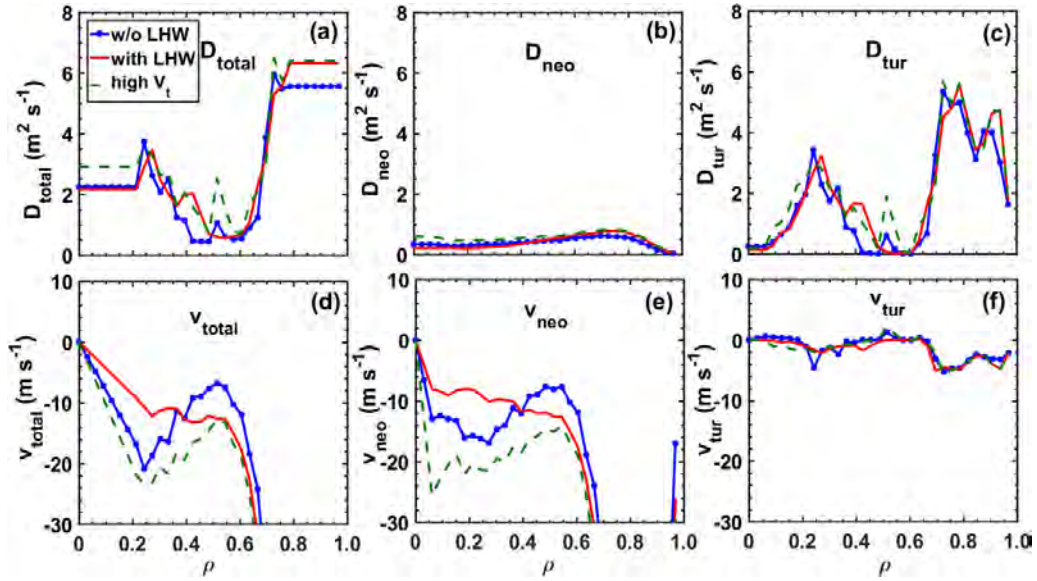
Figure 12. Radial profile of (*a*) total diffusion coefficient, (*b*) neoclassical coefficient, (*c*) turbulent coefficient, (*d*) total pinch velocity, (*e*) neoclassical pinch velocity, (*f*) turbulent pinch velocity calculated by TYGRO. The red solid and blue dot solid line denote the case with LHW switch on and off, respectively. The green dash line shows the transport coefficient calculated for higher toroidal rotation velocity, and other plasma parameter are for case with LHW switch on.
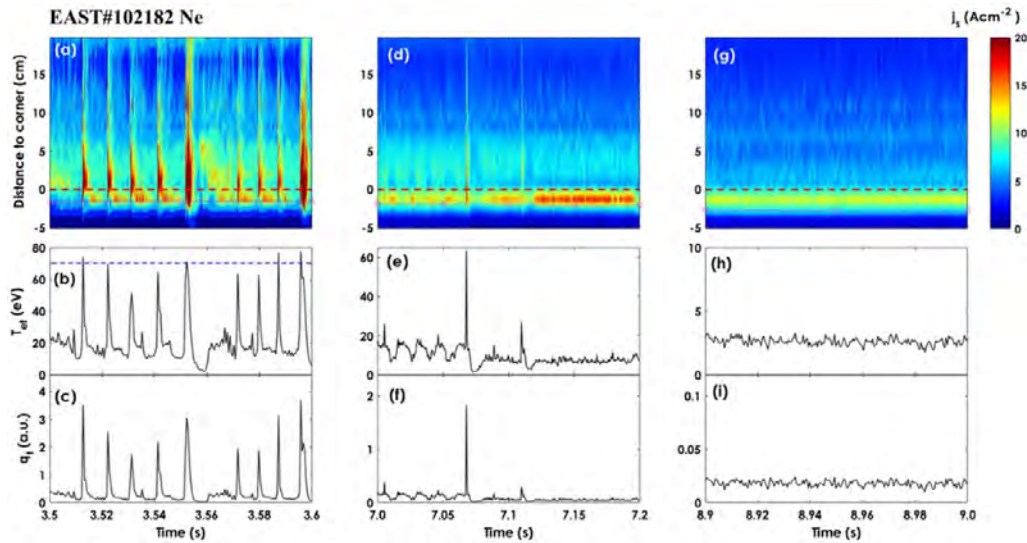
Figure 13. The ion flux density distribution, electron temperature and heat flux around the strike point on the lower outer divertor target measured by Langmuir probe for (*a*)–(*c*) the large ELM phase before Ne seeding, (*d*)–(*f*) the ELM-less phase and (*g*)–(*i*) the ELM-free phase after Ne seeding. Distance to corner means the distance to the interface of vertical and horizontal targets along the target surface.

monotonic with $q_0 < 1$ during sawtooth oscillation to central flat, magnetic shear $s \sim 0$ at $\rho < 0.4$, with fishbone at where off-axis bootstrap current might play a critical role. Linear gyrokinetic simulation by NLT code [26] is qualitatively in good agreement with experimental measurement from CO_2 laser collective scattering. The electron-scale TEM that dominants the transport during sawtooth is found stable with fishbone. In addition, both of increased core ITG and increased density peaking factor would impact the threshold value for micro-instabilities, such as ITG and η_e-driven TEM, and could also play a vital role in the nonlinear process of turbulence saturation. The sustainable improved

confinement during fishbone comparing to the typical sawtooth at the low $q_{95} < 3.5$ operation regime found on EAST could make important contribution to the joint activities of ITER baseline scenario development lead by the ITPA-IOS group [27].

4.2. High beta operation

To further extend the high β_p plasma scenario toward a higher beta and higher f_{bs} regime [28], more neutral beam power is added in the high β_p scenario of the RF-only discharge. Figure 15 shows an example of the high β_p with higher β_N
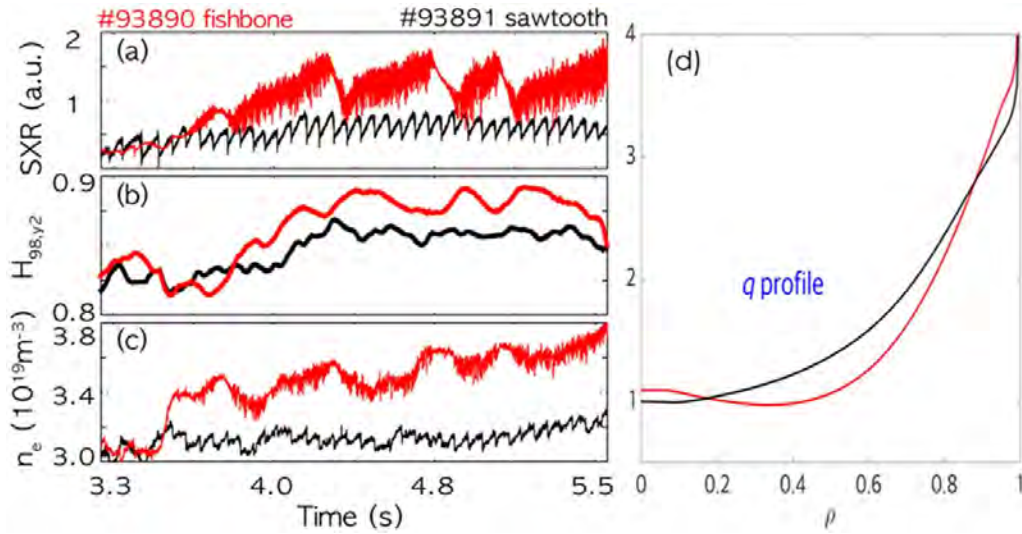
Figure 14. Time evolution of basic plasma parameters for two typical $q_{95} < 3.5$ plasma discharges. (*a*) Soft x-ray emission count, (*b*) energy confinement enhancement factor $H_{98,y2}$ factor and (*c*) line-averaged electron density n_e. (*d*) Comparison of the q profile. Red color represents shot #93890 with fishbone activity and black curves show shot #93891 with sawtooth oscillation.
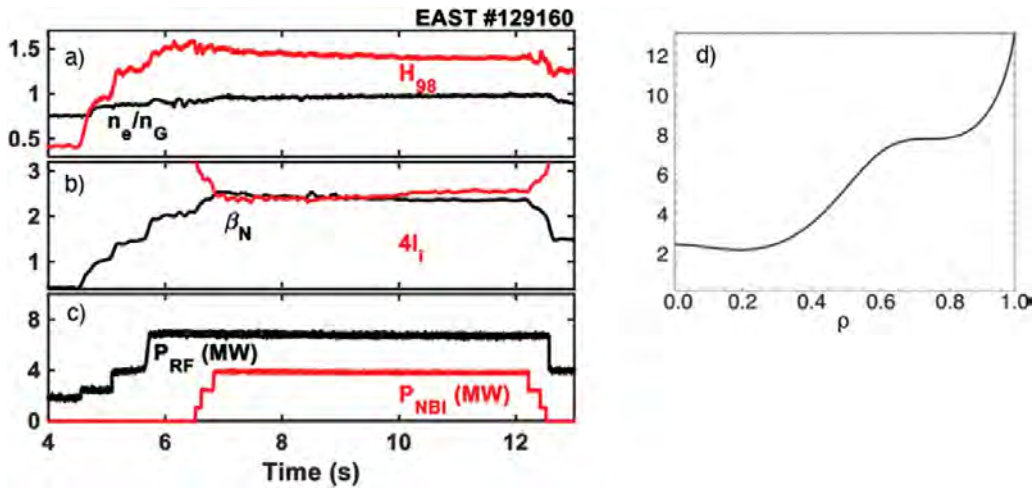
Figure 15. Time traces of high beta H-mode discharge with (*a*) confinement enhancement factor (H_{98y2}), normalized density (n_e/n_{GW}), (*b*) normalized beta (β_N) and $4 \times l_i$, (*c*) injected power of RF (P_{RF}) and NBI (P_{NBI}), (*d*) reconstructed q profile.

plasma discharge ($I_p = 0.3$ MA, $B_T = 2.5$ T, $H_{98y2} > 1.3$, $\beta_P \sim 4.0$, $\beta_N \sim 2.4$, $V_{loop} \sim 0.0$ and $n_e/n_{GW} \sim 1.0$). The β_N value of this discharge reaches $4 \times l_i$, where l_i is the internal inductance calculated from the equilibrium analysis. Note that there is no clear MHD behavior of NTM in the discharge, which is consistent with weak shear of q profile ($q_{min} > 2.0$). Note that the q profile was reconstructed with MSE constraint.

4.3. ELM control

Suppression of type-I ELMs using $n = 4$ resonant magnetic perturbations (RMP) extrapolating favorably to the ITER baseline scenario has been achieved in recent experimental campaigns in EAST. Here n is the toroidal mode number of the applied RMP. EAST has achieved ELM suppression in pure RF heating plasmas for steady state operation with $n = 1$ RMP. To address ITER issues, many studies have been focused on achieving ELM suppression with high n RMPs in low q_{95} and

low NBI input torque plasmas in the last a few years. Full suppression of ELM by using odd parity (opposite phases in the upper and lower rows of coils current) $n = 4$ RMPs in low input torque plasma has been demonstrated for the first time previously in EAST [29]. The advantage of using high n RMPs shown in the experiment is that energy confinement does not obviously drop despite density pump out when ELM suppression is achieved when compared to the ELMy H-mode conditions, while core tungsten concentration is clearly reduced [30]. In previous studies, ELM suppression was only achieved in a narrow q_{95} window ($\Delta q_{95} \sim 0.1$) at around 3.65, which agrees with the position of a resonant peak in plasma response modeled by using the MARS-F code. However, the MARS-F modeling result, as shown in figure 17(*d*), also indicate other resonant peaks including one about $q_{95} \sim 3.1$, which is much closer to the ITER baseline scenario but had not achieved in experiments. The predicted multiple q_{95} resonant windows convince the possibility of extending the ELM suppression to a
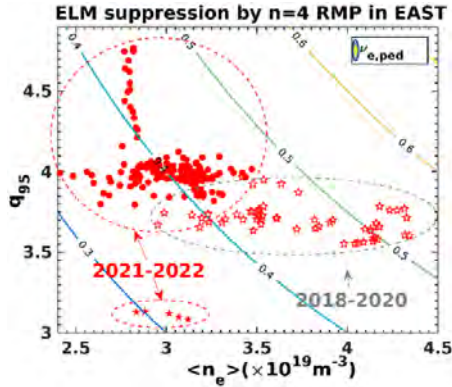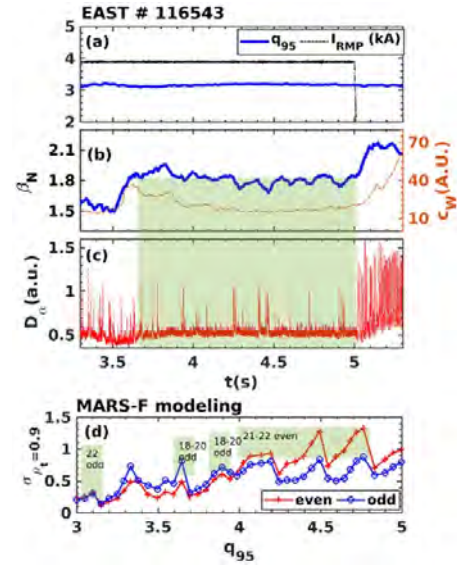
Figure 16. A summary of extension of ELM suppression window with even (red filled circles) and odd parity (red pentagons) $n = 4$ RMPs in the last two years since the last IAEA FEC meeting. The contour line of electron pedestal collisionality is also plotted with the assumption of $T_{e, ped} = 0.6$ keV, $n_{e, ped} = 0.75 \times \langle ne \rangle$, and $Z_{eff} = 1$.

Figure 17. (*a*)–(*c*) From top to bottom are temporal evolution of q_{95} (blue solid line) and $n = 4$ RMP coil current I_{RMP} (black dashed-dotted line), β_N (blue solid line) and tungsten concentration (orange dashed-dotted line) and D_α, and (*d*) MARS-F plasma response modeling results on q_{95} dependence of Chirikov parameter near the pedestal top at $\rho = 0.9$ for odd (blue circles) and even (red pluses) parity $n = 4$ RMP coil configurations. The green areas in (*d*) covers all the ELM suppression q_{95} windows achieved in experiments, which are labeled with the achieved years and RMP coil parity.

much wider operational window. Therefore, significant efforts have been made in recent experiments to extend ELM suppression into a wider q_{95} range [31], especially the lower q_{95} range towards ITER baseline requirements. Remarkable results have been obtained in the last two years in EAST as the achieved ELM suppression window with $n = 4$ RMPs summarized in figure 16. New $n = 4$ RMP ELM suppression windows since 2021 including $q_{95} \sim 3.1$, which is much closer to the ITER baseline scenario, and a much wider q_{95} window from 4.0 to 4.8. These results are all consistent with the MARS-F modeling as shown in figure 17(*d*).

One example of ELM suppression by $n = 4$ odd parity RMP coil configuration at $q_{95} \sim 3.1$ is shown in (*a*)–(*c*) in figure 17. In this experiment, the normalized plasma beta is $\beta_N \sim 1.8$–2.0, which is also close to the ITER 15 MA baseline operational scenario. The toroidal magnetic field strength $B_T \sim 1.5$ T and the line averaged plasma density is around 3.0×10^{19} m^{-3}, which corresponds to 43% of the Greenwald density n_{GW}. The normalized electron collisionality near the pedestal $\nu_{*e,ped}$ is around 0.3, which is also a near-record value for EAST. In this case, the input torque is still only slightly higher than the extrapolated value for 33 MW of NBI in ITER. Therefore, many parameters are very close to the values that expected in the ITER baseline scenario. Good ELM suppression has been achieved when β_N exceeds around 1.8 after one additional beam line switches on at $t = 3.5$ s, although there are still some ELMs occasionally appeared. Tungsten concentration is well controlled during the application of RMPs. The new q_{95} window for ELM suppression confirms well the prediction by MARS-F modeling before the experiment and is located at one of the resonant q_{95} windows for plasma response. Modeling results on q_{95} dependence of plasma response using the MARS-F code [32] are shown in (*d*) in figure 17. Here a series of equilibria with different q_{95} from 3.0 to 5.0 is generated based on a reference equilibrium with $q_{95} \sim 4.0$ by scaling plasma current using CHEASE [33], as in detail explained in [31]. Then these equilibria were used for MARS-F modeling. This was done before the experiment to guide the search for new q_{95} suppression windows and the

selection of coil parity for $n = 4$ RMPs. MARS-F modeling shows that there is a resonant window near $q_{95} \sim 3.1$. However, the amplitude of the Chirikov parameter (indicative of the level of islands overlap) near the pedestal top is much lower than that at $q_{95} \sim 3.65$. This might be the reason of more difficult challenge to access ELM suppression in the experiment at $q_{95} \sim 3$. At this $q_{95} \sim 3$, a high enough plasma beta β_N (~ 1.8) is found to be one of the key factors to enhance the plasma response and hence to achieve ELM suppression. There are multiple resonant windows in plasma response. A much wider window ($\Delta q_{95} \sim 0.6$) at slightly higher q_{95} (~ 4.5) also predicted by MARS-F modeling is confirmed in the experiments in the last two years. All the q_{95} windows achieved in experiments has been covered with green areas and labeled with achieved years and RMP coil parity in figure 17(*d*), which also show the consistency with the peaks predicted by MARS-F.

To further understand the related 3D physics mechanism behind RMP ELM control, various studies of experimental analyses and modelings are carried out. A scaling on threshold density for rotation reversal was also proposed [34, 35]. In EAST experiments, RMP effect on toroidal rotation agrees well with the NTV modeling [36]. RMP effect on tungsten reduction is closely related with rotation braking, and modeling results show that the impact of RMP induced NTV on low charge state tungsten ions is greater than that on high charge state [37]. These promising results expand previous physical understanding and demonstrate the potential effectiveness of RMP for reliably controlling ELMs in the ITER baseline $Q = 10$ scenario.
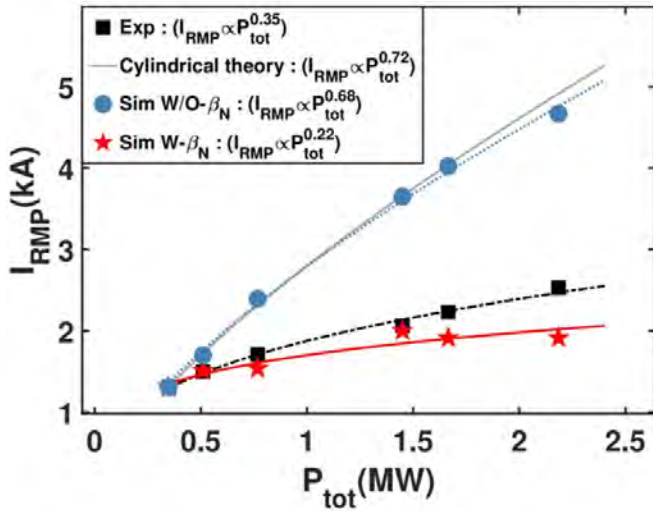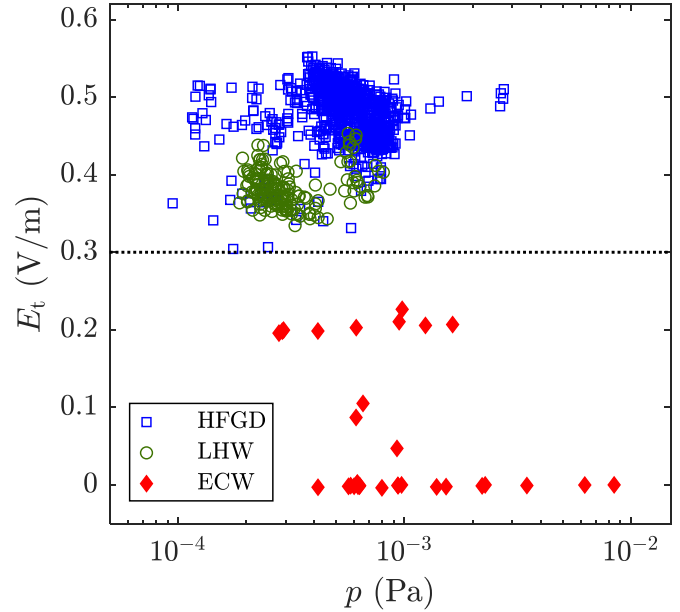
Figure 18. Comparison of the $n = 1$ RMP penetration threshold current scaling with heating power scanning in experiment of $q_{95} = 4.70$ (black scatter points), cylindrical theory (grey solid line), Sim W/O-β_N (blue scatter points) and Sim W-β_N (red scatter points). The dependence of plasma parameter in the heating power scanning used in Sim W/O β_N is $P_{tot} \sim (n_e, T_e, \tau_V, f_0)$ and in Sim W-β_N is $P_{tot} \sim (n_e, T_e, \tau_V, f_0, \beta_N)$.


Figure 19. Parameter domain of EAST breakdown with different pre-ionization methods including high-frequency glow discharge (HFGD), lower hybrid wave (LHW) and electron cyclotron wave (ECW). Breakdown at low toroidal electric field E_t (<0.3 V m^{-1}, the upper limit of ITER) and significant extension of prefilled gas pressure were achieved with ECW pre-ionization.

4.4. Error field analysis

Error field locked mode can limit the high performance operation and even lead to a disruption. Therefore, the clarification scaling differences between theory and experiment are essential. The plasma-beta effect on the $n = 1$ RMP field penetration in purely RF wave heated discharges has been investigated in EAST [38]. The experimental results show that the dependence of the threshold RMP coil current for field penetration, I_{RMPth}, on the total absorbed power P_{tot} scales as approximately $I_{RMPth} \propto P_{tot}^{0.3}$, indicating that the error-field tolerance is improved with increasing RF power. This is benefited by the increased electron perpendicular flow dominated by a counter-current electron diamagnetic flow with increasing RF power. However, theoretical scaling in cylindrical geometry overestimates the power index. Assuming an additional term $\beta^{\alpha n}$ for the normalized beta in the scaling, it is shown that the fitted α_n from the experimental observation is around -1, indicating a degradation effect of plasma beta. To clarify the underlying physics of the plasma-beta effect that was not included in the theoretical scaling in cylindrical geometry, the MARS-Q code [39] with full toroidal geometry is employed for simulation of nonlinear field penetration. The MARS-Q simulation results reproduce the dependence well, and hence the P_{tot} scaling of the threshold current in experimental observations (figure 18).

4.5. EC pre-ionization and assisted startup

Plasma initiation is an essential process of the tokamak operation. During the inductive startup commonly used in tokamaks, the change in the current in central solenoids (CS) induces a toroidal electric field for the neutral gas breakdown

and plasma CD. In superconducting tokamaks, the change rate of the coil current is limited due to the superconductivity. In addition, the eddy current in the thick vacuum vessel delays the penetration of poloidal magnetic field. As a result, the upper limit of the toroidal electric field in a superconducting tokamak is relatively low. For example, the maximum toroidal electric field in ITER will not exceed 0.3 V m^{-1} [40]. Thus, an effective pre-ionization is necessary for breakdown at low toroidal electric field.

Recently, experimental study on electron cyclotron wave (ECW) pre-ionization and assisted startup was carried out on the EAST tokamak with ITER-like superconducting coils and full metal wall. As shown in figure 19, by comparing with other pre-ionization methods including high-frequency glow discharge (HFGD) and LHW, the ECW is capable of pre-ionization to achieve breakdown at low toroidal electric field (<0.3 V m^{-1}). Also, the parameter domain of breakdown is significantly extended towards higher prefilled gas pressure with ECW pre-ionization. The points at 0 V m^{-1} indicate the discharges in which the breakdown (appearance of D_α emission) occurs before the onset of the toroidal electric field, then the plasma current starts to increase as the toroidal electric field appears.

In addition, the effect of electron cyclotron heating (ECH) power on the breakdown was investigated. The result of power scan shows that the lowest ECH power for successful breakdown in EAST is about 400 kW, which is equivalent to about 5 MW in ITER according to extrapolation calculation. The time lags between the ECH application and the D_α emission features like appearance and peak (indicated by $t_{D\alpha}^{appearance}$ and
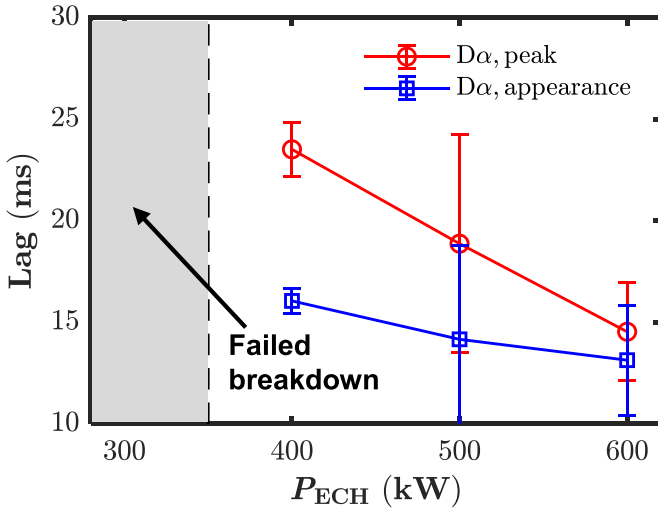
Figure 20. Effect of ECH power P_{ECH} on the time lags between the ECH application and the D_α emission features like appearance and peak indicated by $t_{D\alpha}^{appearance}$ and $t_{D\alpha}^{peak}$, respectively. As P_{ECH} increases, both $t_{D\alpha}^{appearance}$ and $t_{D\alpha}^{peak}$ as well as their difference reduce, which implies that higher ECH power is beneficial to earlier and faster breakdown. In addition, breakdown cannot be achieved with $P_{ECH} = 300$ kW.

$t_{D\alpha}^{peak}$, respectively) were used to evaluate the effect of ECW pre-ionization. The dependence of the time lags on the ECH power is illustrated in figure 20. As ECH power increases, both $t_{D\alpha}^{appearance}$ and $t_{D\alpha}^{peak}$ as well as their difference reduce, which implies that higher ECH power is beneficial to earlier and faster breakdown.

4.6. ITER-like fast ramp down

The termination phase should achieve a simultaneous ramp-down of the plasma current, kinetic energy and particle density while maintaining control over the radiation levels, plasma position and shape, staying within the capabilities of the PF coils, power supplies and heating systems. Generally, ITER will operate with keeping diverted configuration, managing the H–L transition timing, reducing the plasma volume and elongation in termination phase. To validate the assumptions for ITER simulated termination scenarios, plasma control oriented experimental studies have been carried out on EAST. In EAST upper-divertor discharge shot 115672, seen figure 21, the flattop plasma current is 0.45 MA, line-averaged plasma density is 4.5×10^{19} m^{-3}, as shown in figure 21(a). The termination phase starts from 9 s with H mode plasma, H–L transition is managed at 9.5 s with turn-off the LH and EC powers, as shown in figure 21(c). The plasma shape elongation is reduced from 1.75 to 1.3, the vertical instability growth rate is suspended while internal inductance increasing, as shown in figure 21(b). The fastest plasma current ramp-down rate is achieved with 0.33 MA s^{-1} with diverted configuration, as shown in figure 21(d). After scaling to ITER reference scenario with characteristic L/R time constant, a safe ramp-down of the ITER baseline 15 MA discharge with about 0.1 MA s^{-1} plasma current ramp-down rate [41, 42] have been

successfully demonstrated in scaled experiments on the EAST tokamak.

4.7. Material erosion

To enhance the capacity of heat flux, EAST has been upgraded with a new lower W/Cu divertor recently. The flat-type W/Cu structure based on new explosively welding and brazing technologies are expected to withstand high heat loads up to 20 MWm^{-2} on the top surface. A special cooling system structure was designed to increase the heat removal efficiency. Based on previous experiences, large chamfer shaping structures were employed to mitigate the leading-edge-induced high thermal loads. However, melting phenomena have been observed in situ by CCD camera during the long-pulse operation campaign, and identified by post-mortem inspections. Before the occurrence of W melting, debonding of the W plates was already generated by the high thermal stress due to the thermal mismatch between the W plate and CuCrZr substrate, resulting in a residual hot spot after normal discharge. The repetition of this process gradually deteriorated the W/Cu structure and thus resulted in an increased peak temperature until melting occurred [43]. A new structure with a smaller tilt angle ($\sim 2.4°$) can reduce the heat load on the edge-beveled W plate by 36% compared to the previous tilt angle of 5°, which significantly mitigate the melting and exfoliation of W plates [44].

In recent EAST experiments, it is found that W erosion can be suppressed or mitigated by Ne or D_2 gas injection when divertor detachment is obtained. Compared to edge D_2 fueling, Ne seeding from the divertor target is favorable for full detachment condition and thus W erosion suppression. D_2 injection from both divertor target and the outer mid-plane can also induce a partial detachment condition by strongly increase the upstream plasma density, and therefore mitigate the divertor W erosion. With a new developed low-energy neutral particle analyzer (LENPA) [45] and quartz crystal microbalance, material erosion induced by charge-exchange neutrals has been revealed. It is proved that higher density and heating power can increase the flux and energy of neutral particles, which results in higher material erosion rates by neutrals. The measured material erosion rates by neutrals can be well explained by the modeling with the 3D-GAPS codes [46] using the neutral energy spectrum measured by the LENPA system.

5. Summary and future plan

Significant progress has been made in the development and understanding of the relevant physics with respect to the steady state long pulse operation in EAST since the last IAEA-FEC in 2021. A reproducible steady state long pulse H-mode of 403 s with $H_{98y2} > 1.3$ was developed with the integrated operation. To demonstrate the extra long pulse operation capability, a thousand-second time scale (~ 1056 s) fully non-inductive plasma with total energy of 1.73 GJ was obtained. The extension of high β_p, high β_N plasma up to $4 \times$ li was recently
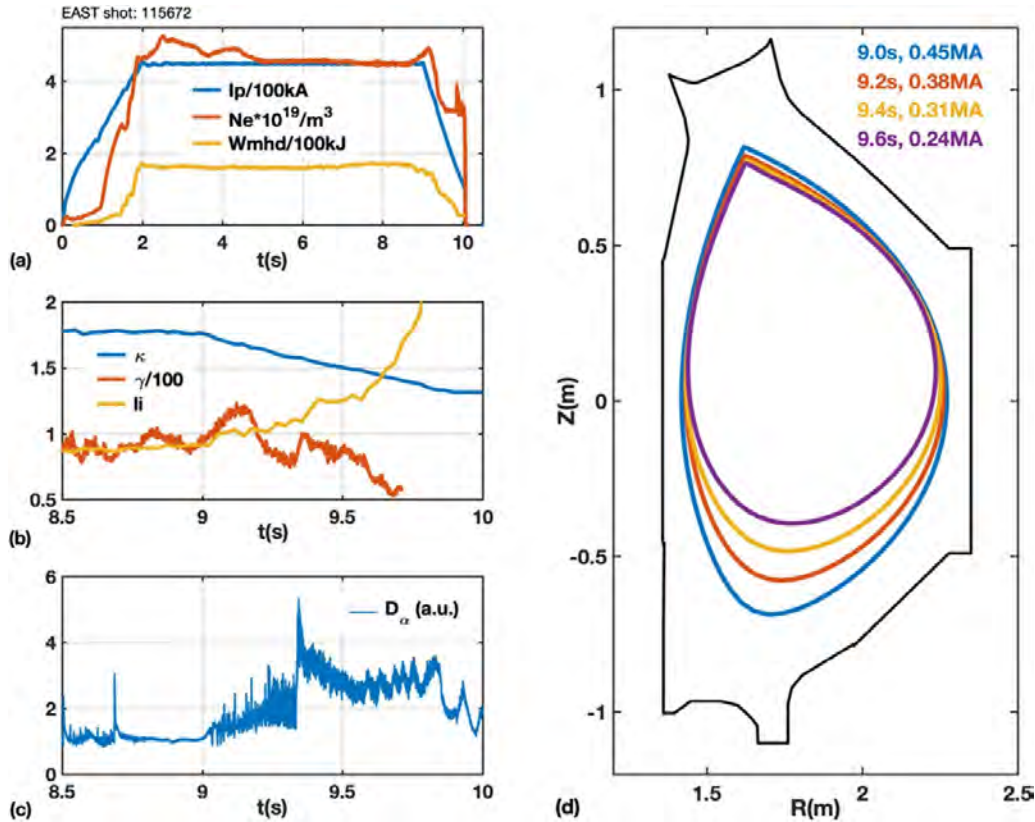
Figure 21. Illustration of controllability of ITER-like fast plasma ramp-down. (*a*) The waveforms of plasma current, density and stored energy (*b*) the waveforms of plasma configuration elongation, vertical displacement instability growth rate and internal inductance during the ramp-down phase (*c*) D_α signal during the ramp-down phase (*d*) the plasma diverted configuration evolution during the ramp-down phase.

achieved. This regime exhibits good compatibility with high confinement, high f_{bs} and fully non-inductive operation.

To support ITER, the ELM suppression by $n = 4$ odd parity RMP coil configuration with $q_{95} \sim 3.1$ is obtained, consistent with the suggested resonant window of MARS-F modeling. The error-field tolerance for field penetration is improved with increasing RF power, i.e. approximately $I_{RMP\,th} \propto P_{tot}^{0.3}$. The use of RMP and on-axis RF heating on the core are demonstrated to the control of tungsten accumulation. Experiments have shown that tungsten erosion can be suppressed or mitigated by Ne or D_2 gas injection when divertor detachment is obtained in EAST. It is found that the ECW is helpful to achieve breakdown at low toroidal electric field ($<0.3\,\mathrm{V\,m^{-1}}$). A fast plasma current ramp-down rate at 0.33 MA s^{-1} is achieved with diverted configuration in EAST.

The near term plans of EAST are to explore 1000 s long-pulse H-mode operation with high bootstrap current fraction and to demonstrate steady-state operation with extended fusion performance. Towards this very long-pulse, high bootstrap current fraction plasma operation, a further extension of the ECH system with two more 105/140 GHz dual frequency gyrotrons is underway and will give a total of 6.0 MW power for heating and profile control. A new 4.6 GHz LHW system will be installed to replace the 2.45 GHz LHW for enhancement of LHCD capability. Meanwhile, the upper divertor will be upgraded to a new full W divertor with closed V-shape configuration for high power exhaust (10 MW m^{-2}) in

supporting the high power long pulse operation. The capability of the water-cooling system will be enhanced with the pressure of 3 MPa. The upgrade of the helium cooling system operational temperature from 4.5 K to 3.8 K will increase the poloidal coil's current limit by 10–15%, leading to a higher plasma current platform ($I_p \leqslant 1.0$ MA). In addition, more NB power will be available with new ion source up to 120 keV, facilitating to study AE physics. All these enhancements will further strengthen EAST as a key facility for steady state long pulse operation and physics research for future devices.

Acknowledgments

References

[1] Wan B.N. *et al* 2019 *Nucl. Fusion* **59** 112003
[2] Wan B.N. *et al* 2022 *Nucl. Fusion* **62** 042010
[3] Rodriguez-Fernandez P. *et al* 2022 *Nucl. Fusion* **62** 042003
[4] Gormezano C. *et al* 2007 *Nucl. Fusion* **47** S285

[5] Song Y. *et al* 2023 *Sci. Adv.* **9** 1
[6] Whyte D.G. *et al* 2010 *Nucl. Fusion* **50** 105005
[7] Sun Z. *et al* 2019 *Nucl. Mater. Energy* **19** 124
[8] Li M.H. *et al* 2023 *Nucl. Fusion* **63** 046019
[9] Yang H. *et al* 2021 *Nucl. Fusion* **61** 035001
[10] Zhang X.J. *et al* 2022 *Nucl. Fusion* **62** 086038
[11] Yuan Q.P. *et al* 2013 *Nucl. Fusion* **53** 043009
[12] Huang Y. *et al* 2020 *Nucl. Fusion* **60** 076023
[13] Guo Y., Wang Y.H., Xiao B.J., Liu L., Qiu Q.L. and Yang F. 2020 *Nucl. Fusion* **60** 076002
[14] Albanese R., Ambrosino R., Castaldo A., De Tommasi G., Luo Z.P., Mele A., Pironti A., Xiao B.J. and Yuan Q.P. 2017 *Nucl. Fusion* **57** 086039
[15] Chen D., Biao S.H., Tonghui S.H., Bihao G.U., Tingyu L.I., Lixing C.H., Minmin X.U. and Nan C.H. 2023 *Plasma Sci. Technol.* **25** 125102
[16] Shi S. *et al* 2022 *Nucl. Fusion* **62** 066032
[17] Cheng Y. *et al* 2022 *Rev. Sci. Instrum.* **93** 123501
[18] Shi S. *et al* 2022 *Nucl. Fusion* **62** 066031
[19] Li K.D. *et al* 2021 *Nucl. Fusion* **61** 066013
[20] Meng L.Y., Xu J.C., Liu J.B., Cao L., Wang P., Li A., Yu L., Xu G.S. and Wang L. 2022 *Fusion Eng. Des.* **175** 113011
[21] Tao Y.Q. *et al* 2023 *Nucl. Fusion* **63** 076008
[22] Wang L. *et al* 2022 *Nucl. Fusion* **62** 076002
[23] Li K.D. *et al* 2023 *Nucl. Fusion* **63** 026025
[24] Yang X. *et al* 2024 *Nucl. Fusion* **64** 016030
[25] Zhang B. *et al* 2022 *Nucl. Fusion* **62** 126064
[26] Ye L., Xu Y., Xiao X., Dai Z. and Wang S. 2016 *J. Comput. Phys.* **316** 180
[27] Sips A.C.C. *et al* 2018 *Nucl. Fusion* **58** 126010
[28] Huang J. *et al* 2019 *Plasma Phys. Control. Fusion* **62** 014019
[29] Sun Y. *et al* 2021 *Nucl. Fusion* **61** 106037
[30] Jia M. *et al* 2021 *Nucl. Fusion* **61** 106023
[31] Xie P. *et al* 2023 *Nucl. Fusion* **63** 096025
[32] Liu Y., Kirk A. and Nardon E. 2010 *Phys. Plasmas* **17** 122502
[33] Lütjens H., Bondeson A. and Sauter O. 1996 *Comput. Phys. Commun.* **97** 219
[34] Li H., Sun Y., Wang L., He K. and Shaing K.-C. 2021 *Nucl. Fusion* **61** 104002
[35] Li H., Sun Y. and Wang L. 2023 *Phys. Plasmas* **30** 052504
[36] Sheng H. *et al* 2023 *Nucl. Fusion* **63** 076002
[37] Chang Y. *et al* 2023 *Phys. Plasmas* **30** 122301
[38] Ye C. *et al* 2023 *Nucl. Fusion* **63** 076004
[39] Liu Y., Kirk A. and Sun Y. 2013 *Phys. Plasmas* **20** 042503
[40] ITER Physics Expert Group on Disruptions, Plasma Control, and MHD 1999 *Nucl. Fusion* **39** 2577
[41] de Vries P.C. *et al* 2018 *Nucl. Fusion* **58** 026019
[42] Gribov Y., Kavin A., Lukash V., Khayrutdinov R., Huijsmans G.T.A., Loarte A., Snipes J.A. and Zabeo L. 2015 *Nucl. Fusion* **55** 073021
[43] Zhu D. *et al* 2023 *Nucl. Fusion* **63** 036022
[44] Guo Z., Zhu D., Li C., Wang B., Ding R., Xuan C., Gao B., Yu B., Wang Y. and Chen J. 2023 *Nucl. Mater. Energy* **37** 101524
[45] Mu L., Ding R., Zhu Y.B., Chen J.L. and Li S. 2018 *Rev. Sci. Instrum.* **89** 10I117
[46] Shi X.Z., Ding R., Matveev D., Mu L., Liu N.X., Xie H., Xu G.L. and Chen J.L. 2023 *Nucl. Fusion* **63** 066015